A Finite Wavelet Domain Method for the Rapid Analysis of Transient Dynamic Response in Rods and Beams

C.V. Nastos, T.C. Theodosiou, C.S. Rekatsinas and D.A. Saravanos[1]

Abstract: A computationally efficient numerical method is developed for the prediction of transient response in orthotropic rod and beam structures. The method takes advantage of the outstanding properties of compactly supported Daubechies wavelet scaling functions for the spatial approximation of displacements in a finite domain of the structure, hence is termed Finite Wavelet Domain (FWD) method. The basic principles and advantages of the method are presented and the discretization of the equations of motion is formulated for one-dimensional structures. Numerical results for the simulation of propagating guided waves in rods and strips are presented and compared against traditional finite elements.

Keywords: Daubechies Wavelets, Wavelet-based Elements, Numerical Analysis, Dynamic Transient Response, Meshless

1   Introduction

The dynamic transient response and wave propagation in structural components has attracted substantial interest in many application areas, including the development of innovative Nondestructive Evaluation (NDE) and Structural Health Monitoring (SHM) methods and systems, the simulation of impact events, and so forth. Of particular importance is the design of passive and active SHM systems based on linear and nonlinear guided waves, which require quick and robust simulations of ultrasonic wave propagation in pristine and damaged structures. Guided ultrasonic waves entail very high frequencies and wavenumbers and their numerical solution requires very fine spatial and temporal discretization. Such analyses based on well-established finite element methods (FEM) and finite difference methods (FDM) are computationally expensive and suffer from numerical shortcomings. Thus, there is an emerging need for development of new modeling methods which can provide solutions of substantially improved computational speed and accuracy.

---

[1] Corresponding Author: Professor D.A.Saravanos, saravanos@mech.upatras.gr, Tel: +30-2610-969437, Fax: +30-2610-969417

Over the past decades, various numerical methods and techniques have been proposed for the simulation of guided wave propagation phenomena in solid structures. Finite element method (FEM) [Bathe (1996)], Finite Difference Method (FDM) [Strikwerda (2004)] and Boundary Element Method (BEM) [Katsikadelis (2002)] have long histories in wave propagation. Spectral Element Method (SEM) combines the geometrical flexibility of standard low-order FEM, with rapid convergence properties [Patera (1984)]. The Mass-Spring Lattice Models (MSLM), model the inertia of the analyzed medium using mass particles; the stiffness is modelled using spring elements connecting the mass particles and employs the framework of the Local Interaction Simulation Approach (LISA) [Delsanto and Scalerandi (1998)].

The present paper presents a new approach, which implements Wavelet Scaling Functions (WSF) for the spatial approximation of the displacement fields and explores its potential for the solution of wave propagation problems in elastic rods and 1D and 2D generalized beam models. Numerous wavelets exist in literature, but the Daubechies (DB) family [Daubechies (1992)] is chosen in the present work because it exhibits unique properties as a functional basis: (1) compact support which enables the development of a meshless method with a finite localized domain of influence and provides banded matrices; (2) orthonormality, which can yield diagonal or nearly-diagonal consistent mass matrices thus facilitate and speed-up the utilization of explicit integration methods; and (3) maximum number of vanishing moments for a given order, compared to any other wavelet family. Numerous works have appeared in the past exploiting wavelets/WSFs as basis functions for the solution of differential equations and boundary value problems [Monasse and Perrier (1998); Qian and Weiss (1993); Dempster and Eswaran (2001)]. Integration of wavelet theory into FEA has also been successfully demonstrated. Patton and Marks [Patton and Marks (1995b,a)] have demonstrated the superiority of wavelet-based FEA vs. traditional approaches using a rod element in static and free vibration problems. Ma, Xue, Yang and He [Ma, Xue, Yang, and He (2003)] have constructed a wavelet-based beam element by using DB scaling functions and suggested a way for transforming wavelet coefficients into nodal displacements and rotations. Diaz, Martin and Vampa [Díaz, Martín, and Vampa (2009)] have applied DB wavelets as interpolating shape functions to construct an Euler-Bernoulli beam element and a Mindlin-Reisner plate element for static analysis. Ko, Kurdila and Pilant [Ko, Kurdila, and Pilant (1995)] have developed a class of finite elements based on compactly supported and shift-invariant functions. In a different direction, Mitra and Gopalakrishnan [Mitra and Gopalakrishnan (2005)] have developed wavelet based spectral finite elements for studying wave propagation by converting the wave equation to a system of ordinary differential equations using DB wavelet

approximation in time. Also wavelet element models for damage detection, using Hermite cubic spline wavelets have been designed [Xiang, Matsumoto, Wang, and Jiang (2011); Xiang, Wang, Jiang, Long, and Ma (2012); Xiang and Liang (2011)]. In the following sections, a new method is described focusing on the numerical solution of transient structural dynamic problems. The introduced method, termed as Finite Wavelet Domain (FWD) method, exploits the compactly supported nature of WSFs. The spatial interpolation is introduced in 1D form and is shown to result in a meshless discretization which include a finite set of grid points. Each grid point is affected by a domain of influence determined by WSF support. The discretization formulation follows the Galerkin approach in a way similar to the displacement-based FEM. Consistent mass and stiffness matrices for rod, shear beam and higher order generalized beam models are derived. The transient response is predicted using the central-differences explicit time integration scheme. Although the use of wavelet functions seems very promising, various computational challenges are also arising. The most important are the lack of explicit expressions for the DB family and their highly oscillatory nature, which hinders the implementation of numerical integration in variational formulations and results in ill-conditioned matrices. Numerous reported works are exploited in this paper to overcome such limitations. The paper is organized as follows: Section 2 introduces basic concepts of wavelet theory and properties of the Daubechies WSF family; Section 3 extensively describes the concept of the method, its basic features and the construction of a rod and both a first-order and high-order shear beam element; Section 4 presents numerical examples of wave propagation analyses in rods and beams, convergence evaluations and comparisons with traditional FEA [Theodosiou, Nastos, Rekatsinas, and Saravanos (2014)]. The superiority of the FWD method compared to traditional FEA in terms of accuracy, convergence rate, refinement capabilities, and computational efficiency is quantified.

2 Theoretical Background

The selection of the most suitable WSF as interpolating function is an issue of much discussion [Kessler, Payne, and Polyzou (2008)]. Numerous wavelet families exist, each one with special characteristics. The Daubechies WSFs family seems to be advantageous [Daubechies (1992); Lin, Kovvali, and Carin (2005)] for the approximation of state variables and the solution of variational forms of equations of motion, because they exhibit unique properties as functional bases, summarized below. The family of compactly supported orthonormal wavelet scaling functions $\phi(x)$ constructed by I. Daubechies, includes members of variable smoothness, ranging from highly unsmooth to highly smooth functions of different order. As seen in Figs. 1-3, each parent member is nested at the point $x = 0$ and spans over a

range of grid points, termed the support domain. By definition, every WSF vanishes beyond its support domain.
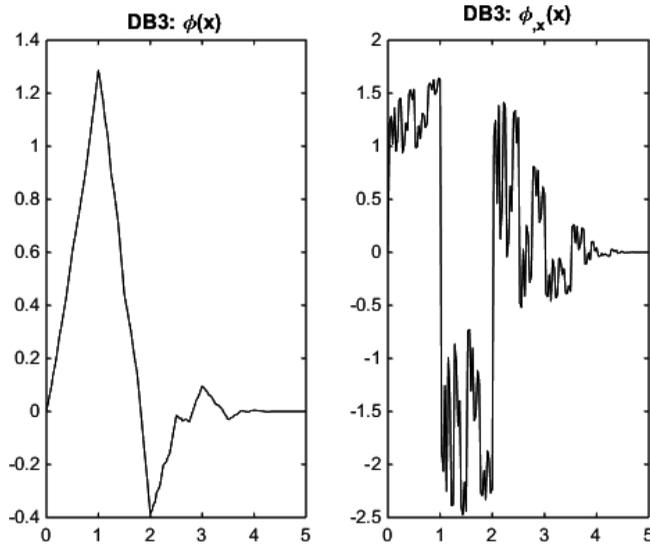
Figure 1: DB3 Scaling function and its Derivative.
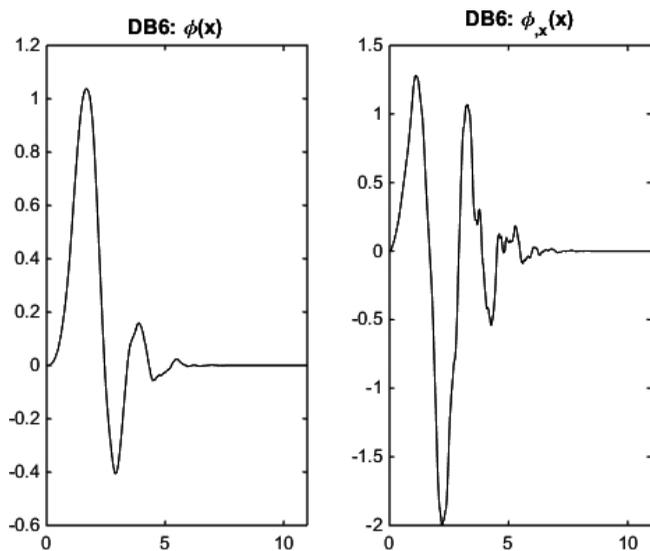
Figure 2: DB6 Scaling function and its Derivative. (Finish Line with Dot)

Additional scaling functions of the same order can be defined either by translating the parent WSF at other integer points j, thus creating new WSFs of the type
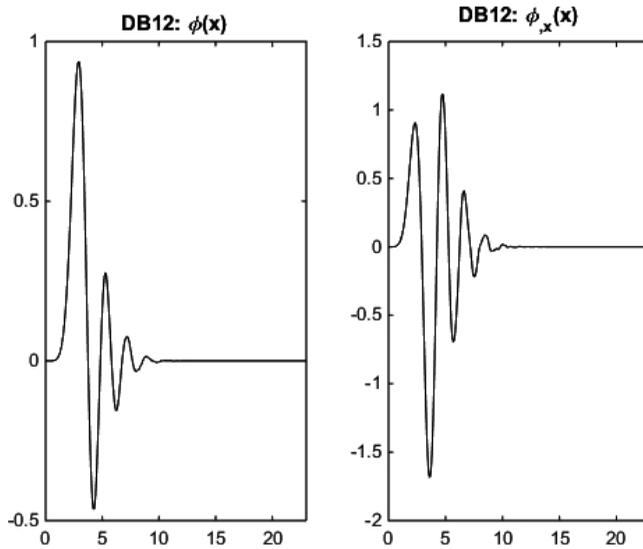
Figure 3: DB12 Scaling function and its Derivative. (Finish Lie with Dot)

$\phi\,(x-j)$; or by shrinking/dilating the parent function to new WSFs $\phi\left(2^{j}x\right)$, respectively. In addition, the following properties are of paramount importance to the application of WSF as interpolation functions:

Compact support. Each WSF and its integer translates are confined within a bounded interval, which spans over a finite range of adjacent grid points. The value of the WSF beyond its compact support is zero by definition. Thus, the influence of a WSF as interpolation function is localized within the interval of compact support. The size of the interval of compact support depends on the order of the parent WSF.

Orthonormality. The integer translates of the WSF are orthonormal to each other, hence, the integer translates of WSFs form an orthonormal basis in the functional space.

$$\int_{-\infty}^{\infty}\phi\,(x-i)\cdot\phi\,(x-j)\,dx=\delta_{ij} \tag{1}$$

Vanishing Moments. The number of vanishing moments defines the quality of the approximation, since it indicates the maximum degree of polynomial function that can be exactly approximated by a specific WSF. The current paper is focused on the well-established Daubechies family. A DB WSF of order L has vanishing moments, which is among the highest regarding common wavelet families [Burgos, Santos, and e Silva (2013, 2015)].

Dilation Property. The final important property of WSF is provided by the dilation

equation,

$$\phi\left(2^j x\right) = \sqrt{2} \cdot \sum_{k=0}^{L-1} h_k \cdot \phi\left(2^{j+1}x - k\right) \tag{2}$$

where h_k is the set of *L filter coefficients*, with L being the order of the wavelet. The property is unique, in the sense that it provides a relationship between the scaling function of a coarse approximation scale ($j = 0$) with the WSF of a finer approximation ($j = 1$). The dilatation property provides the basis for the calculation of WSF values at dyadic points and the calculation of integrals later used and shown in the Appendix. The dilation property is also employed for the forward and inverse wavelet transform.

3   The Finite Wavelet Domain Method

In the present section the basic concepts of the FWD method are presented for the case of 1D problems. The approximation of displacements employing Daubechies WSFs as basis functions is described and its advantages are enumerated. The method is applied to the solution of transient dynamic wave problems in rods, Timoshenko shear beams and High Order beams [Rekatsinas, Nastos, Theodosiou, and Saravanos (2014, 2015)].

3.1   Generalized Approximation of Field Variables

Figure 4 depicts the proposed approximation of a generalized 1D problem. A rod or beam structure of physical length l has been divided into N segments using $N + 1$ grid points, termed as nodes. The segment length practically defines the scale of the approximation and is used for the calculation of the basic stiffness and mass matrices, thus, each segment can be thought as a special element. Additional $L - 1$ nodes are introduced to the left of the physical domain. The case of a DB3 WSF has been selected in Figure 4 for demonstration purposes, but generalized descriptors are used in order to preserve generality.
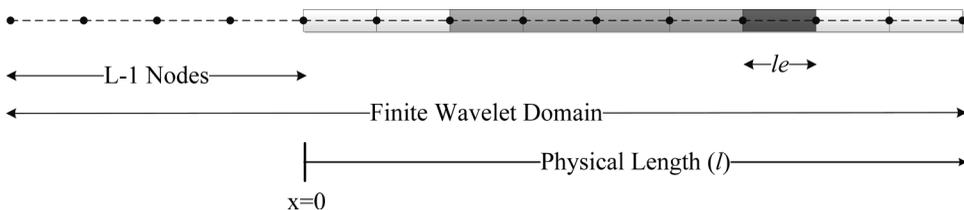
Figure 4: Discretization of Total Domain. (Finish Line with Dot)

Assuming that the nodes coincide with the main dyadic points, the physical displacements $u(x,t)$ can be approximated as,

$$u(x,t) = \sum_{n=-\infty}^{\infty} \hat{u}_n(t) \cdot \phi(\xi - n), \, n \in \mathbb{Z}, \, \xi, t \in \mathbb{R}^{\geq 0} : 0 \leq x \leq l \tag{3}$$

where: x,t are the spatial and time variable, respectively; L is the order of WSF; l the physical length; $\phi(x-n)$ are integer translates of the WSF interpolation function; $\hat{u}_n$ are a set of unknown coefficients to be determined. The later denote the projection of the physical degrees of freedom into the wavelet space. A normalized local coordinate system is associated with each element (Figure 5). The relation between the global coordinate x to the local non-dimensional coordinate is provided by

$$\xi = \frac{x - x_i}{x_{i+1} - x_i} \tag{4}$$
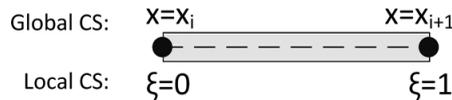
Figure 5: Global vs. Local Coordinate System.

Since WSFs are compactly supported, there is only a limited number of nodes that need to be considered for the approximation of the physical displacement within each element in the context of Eq. (3). Thus, in the interval between subsequent two-grid points, the displacement approximation is reduced to

$$u(x,t) = \sum_{n=-(L-2)}^{0} \hat{u}_n(t) \cdot \phi(\xi - n) \tag{5}$$

where $0 \leq x \leq l_e$ and $0 \leq \xi \leq 1$. The summation limits are confined in the range determined by the order L of the scaling function. Clearly, the approximation in a single element is supported within $L-1$ nodes, as illustrated in Figs. 4 and 6. This 'Finite Wavelet Domain' (FWD) of Influence has inspired the employed terminology, thus each element is termed thereafter as a FWD Element. The approximation over the total length of the structure is obtained by contributions of all elements.

At this point, some important advantages of the FWD method vs. the traditional FEM can be highlighted. The FWD approximation of a field variable in an element requires a range of nodes beyond the physical element range, while in traditional
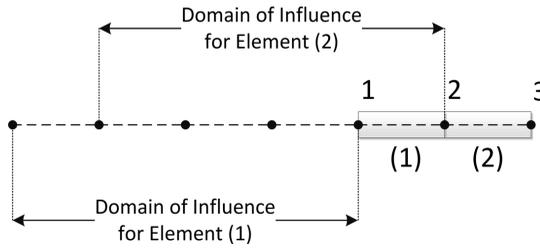
Figure 6: The Domain of Influence for a FWD Element.

FEA the approximation is local and strictly confined within each element; i.e. the displacement field in the interior of a FE is determined only by the nodal displacements of the respective FE. On the other hand, FWD method exploits the overlap of the influence domain for each element (Figure 6) and FWD elements use nodal displacements of previous elements as well. In fact, the amount of nodal information utilized for the approximation of a field variable within an element is larger than any traditional FE of the same approximation order. The amount of nodal information depends on the size of the influence domain, which in turn depends on the order of the selected wavelet. Apparently, the obtained FWD approximation lies between the global Ritz type approximation and local FEM approximation, hence, it is expected to blend advantages of both. The FWD can improve the quality of approximation using either the *h-method* (keeping the order of interpolation functions fixed and decreasing the nodal distance h) or the *p-method* (keeping the nodal distance fixed and increasing the order p of the polynomial approximation). Due to the vanishing moment property of the WSF, an increase in the order of a DB WSF in Eqs. (3) or (5), is related to a measurable improvement in the order of polynomial approximation. Specifically, an increment in the polynomial order of approximation requires increasing the order *L* of the interpolating WSF by a factor of 2. This increase requires only a simple addition of only two external nodes. In practice, no remeshing is required in the physical domain; two external nodes are added leaving the existing internal grid unchanged. On the contrary, in FEM, an increment of the polynomial order of approximation requires the addition of one node per element and full remeshing of the physical domain with new finite elements.

The equation of motion is based on the principle of virtual displacements for a two-dimensional solid defined in terms of axial and transverse coordinates. Taking advantage of the discretization of the physical domain in grid intervals (Figure 4), the fore mentioned FWD elements, the equation of motion can be recast as

$$\sum_{i=1}^{NrElements} \int_0^{l_e} \left(\int_{-\frac{h}{2}}^{\frac{h}{2}} \delta\boldsymbol{\varepsilon}^{\mathbf{T}}\boldsymbol{\sigma}\,dz - \int_{-\frac{h}{2}}^{\frac{h}{2}} \delta\mathbf{u}^{\mathbf{T}}\rho\ddot{\mathbf{u}}\,dz + \left[\delta\overline{\mathbf{u}}^{\mathbf{T}}\overline{\tau}\right]_{-\frac{h}{2}}^{\frac{h}{2}} \right) dx = 0 \tag{6}$$

where: $\boldsymbol{\sigma}$ and $\boldsymbol{\varepsilon}$ are the stress and strain respectively, u are the displacements, τ are the distributed forces and overbar indicates quantities on the boundary using extended vector notation; h is the thickness or normalized area of the structure. Combining Eqs. (5) and (6), equivalent stiffness $[K_e]$ and mass $[M_e]$ matrices, as well as surface traction vectors can be calculated for each FWD element; there are defined in

$$\delta \hat{U}_e^T \cdot [K_e] \cdot \hat{U}_e = \int_0^{l_e} \int_{-\frac{h}{2}}^{\frac{h}{2}} \delta \varepsilon^T \boldsymbol{\sigma} \, dz dx \tag{7}$$

$$\delta \hat{U}_e^T \cdot [M_e] \cdot \ddot{\hat{U}}_e = \int_0^{l_e} \int_{-\frac{h}{2}}^{\frac{h}{2}} \delta u^T \rho \ddot{u} \, dz dx \tag{8}$$

$$\delta \hat{U}_e^T \cdot \boldsymbol{F}_{\tau e} = \int_0^{l_e} \left[\delta \overline{u}^T \cdot \overline{\tau} \right]_{-\frac{h}{2}}^{\frac{h}{2}} dx \tag{9}$$

where $\hat{U}_e$ is the vector of wavelet coefficients involved in the elemental approximation of the displacements in Eq. (5). The total matrices can be assembled from all elemental contributions using typical FEA procedures, which finally provide the discrete equations of motion expressed in the wavelet space:

$$[M] \cdot \ddot{\hat{U}}(t) + [K] \cdot \hat{U}(t) = \boldsymbol{F}(t) \tag{10}$$

In Eq. (10), $[M], [K]$ are the total mass/stiffness matrices respectively, $\boldsymbol{F}$ is the external load vector and is the vector containing all unknown wavelet coefficients in Eq. (3).

3.2 Developement of a FWD Rod Element

Application of the FWD method is primarily demonstrated by considering the analysis of the axial transient dynamic and wave propagation response in an elastic rod governed by the well-known wave equation of motion,

$$u_{,xx} = \frac{\rho}{E} \ddot{u} - b_x \tag{11}$$

where, u is the uniform axial displacement in a cross-section of the rod, subscript ",x" and overdot indicate spatial and temporal derivatives respectively; ρ is the material density; E is the Young modulus of the rod; and b_x represents the distributed axial forces. Assuming arbitrary variation of displacement, the Virtual Work Principle provides the variational form of the previous equation of motion,

$$-\int_0^l \delta \varepsilon_x \cdot \sigma_x \cdot A dx - \int_0^l \delta u \cdot (\rho \ddot{u}) \cdot A dx + \int_0^l \delta u \cdot b_x \cdot A dx + \delta \overline{u} \cdot \bar{\sigma}_x \cdot A \mid_0^l = 0 \tag{12}$$

where, σ_x and ε_x are the axial stress and strain respectively, A is the cross-sectional area and overbar indicates quantities on the boundary. Taking into account Eq. (5), the axial strain is approximated by:

$$\varepsilon_x(x,t) = u_{,x}(x,t) \approx \frac{1}{l_e} \sum_{n=-(L-2)}^{0} \hat{u}_n(t) \cdot \phi_{,\xi}(\xi - n) \tag{13}$$

Incorporating Hooke's law

$$\sigma_x = E \cdot \varepsilon_x \tag{14}$$

into Eq. (12) and substituting Eq. (13) into the equation of motion, Eq. (12) yields the stiffness matrix $[\boldsymbol{K_e}]$, the mass matrix $[\boldsymbol{M_e}]$ and the load vector $\boldsymbol{F_e}$ for an arbitrary FWD element. Taking advantage of the local coordinate system the integration interval is reduced to $[0,1]$, thus stiffness/mass matrices and load vector can be explicitly cast in the wavelet space as

$$[\boldsymbol{K_e}] \equiv \left[K^{kl}\right] = \frac{EA}{l_e} \int_0^1 \phi_{,\xi}(\xi - k) \cdot \phi_{,\xi}(\xi - l)\, d\xi = \frac{EA}{l_e}\left[\Gamma_{kl}^{11}\right] \tag{15}$$

$$[\boldsymbol{M_e}] \equiv \left[M^{kl}\right] = \rho A l_e \int_0^1 \phi(\xi - k) \cdot \phi(\xi - l)\, d\xi = \rho A l_e \left[\Gamma_{kl}^{00}\right] \tag{16}$$

$$[\boldsymbol{F_e}] \equiv \left[F^k\right] = A l_e \int_0^1 b_x \cdot \phi(\xi - k)\, d\xi = b_x A l_e R_k^0 \tag{17}$$

where, Γ_{kl}^{00}, Γ_{kl}^{11} and R_k indicate respective wavelet connectivity coefficients defined in the Appendix.

Additional advantages of the FWD method are realized in the synthesis of the mass matrix. Due to the compact support of the WSFs, the stiffness matrices are symmetric, sparse and narrow-banded, which enables fast and accurate solution of large-size static [Li and Chen (2014)] and dynamic problems. Furthermore, the orthonormality of WSFs combined with their compact support yields a nearly diagonal consistent mass matrix $[\boldsymbol{M}]$ in Eq. (16). As an example, Figure 7 depicts the pattern of non-zero terms in the mass matrix of a rod a structured modeled with N FWD elements of order L.

3.3   Developement of a FWD Shear Beam Element

The previous formulation is further extended to the transient dynamic analysis of Timoshenko shear beams, i.e. to include axial extensional and rotational inertia terms. Compared to the previous case of simple rods, the analysis of shear beams induces two major challenges: (i) Additional field variables are introduced, which
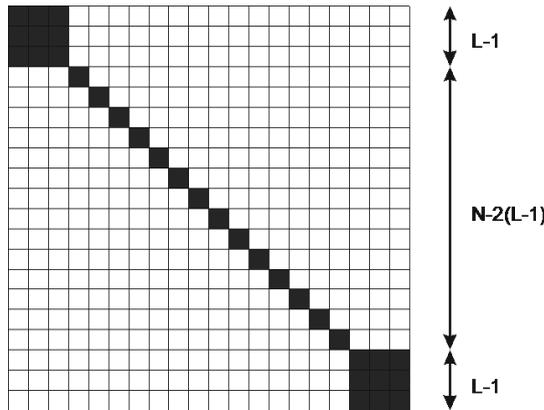
Figure 7: Typical pattern of non-zero terms in the mass matrix of the rod FWD method for the case of N elements and L order scaling functions.

can capture both the longitudinal and the first antisymmetric (A_0) guided wave mode; and (ii) The application of shear beam FEs in transient dynamic problems suffers from well-known numerical problems, such as "shear locking" which is usually treated with reduced integration and spurious "hour-glass" modes.

According to the first order shear beam theory, the axial and transverse displacement, u and w respectively, of the cross-section are

$$u(x,z,t) = u^0(x,t) + \beta_x(x,t) \cdot z \tag{18}$$
$$w(x,z,t) = w^0(x,t) \tag{19}$$

where u_0 and w_0 are the axial and transverse displacement at the midplane of the beam; β_x is the rotation of the cross-section; and z is the local thickness coordinate. The axial (ε_x) and shear (ε_{xz}) strains

$$\varepsilon_x(x,z,t) = \varepsilon_x^0(x,t) + k_x(x,t) \cdot z \tag{20}$$
$$\varepsilon_{xz}(x,z,t) = \varepsilon_{xz}^0(x,t) \tag{21}$$

are described in terms of the generalized strains $\varepsilon_x^0 = u^0{}_{,x}$, $k_x = \beta_{x,x}$ and $\varepsilon_{xz}^0 = \beta_x + w^0{}_{,x}$. The equivalent Hooke's law for the generalized stresses and strains of a beam cross-section has the form

$$\begin{Bmatrix} N_x \\ N_{xz} \\ M_x \end{Bmatrix} = \begin{bmatrix} A_{11} & 0 & 0 \\ 0 & A_{55} & 0 \\ 0 & 0 & D_{11} \end{bmatrix} \cdot \begin{Bmatrix} \varepsilon_x^0 \\ \varepsilon_{xz}^0 \\ k_x \end{Bmatrix} \tag{22}$$

where N_x, N_{xz}, M_x are the axial forces, the shear forces and the bending moment respectively; A_{11}, A_{55}, D_{11} are the extensional, shear and flexural stiffness of the

cross-section. The equation of motion provided by the Virtual Work Principle is

$$-\int_0^l \left(\delta\varepsilon_x^0 \cdot N_x + \delta\varepsilon_{xz}^0 \cdot N_{xz} + \delta k_x^0 \cdot M_x\right) dx + \int_0^l \delta\boldsymbol{u}^T \cdot \boldsymbol{\rho} \cdot \ddot{u} dx + \oint_S \delta\bar{\boldsymbol{u}}^T \cdot \bar{\tau} dS = 0 \quad (23)$$

where $\boldsymbol{u} = \left[u^0, w^0, \beta_x\right]^T$ are the generalized displacements of the cross section; $\boldsymbol{\rho} = diag\left(\rho^A, \rho^A, \rho^D\right)$ is the density matrix containing the linear density (ρ^A) and rotational inertia (ρ^D); $\bar{\tau}$ are the surface tractions on the boundary S. Expanding Eq. (5), the generalized state variables of the beam are approximated within an WFD element

$$\begin{Bmatrix} u^0 \\ w^0 \\ \beta_x \end{Bmatrix} = \sum_{n=-(L-2)}^{0} \begin{Bmatrix} \hat{u}_n^0 \\ \hat{w}_n^0 \\ \hat{\beta}_{xn} \end{Bmatrix} \cdot \phi\left(\xi - n\right) \quad (24)$$

while the approximation of generalized strains in an element takes the form

$$\begin{Bmatrix} \varepsilon_x^0 \\ \varepsilon_{xz}^0 \\ k_x \end{Bmatrix} = \sum_{n=-(L-2)}^{0} \begin{bmatrix} \phi_{,\xi}\left(\xi - n\right) & 0 & 0 \\ 0 & \phi_{,\xi}\left(\xi - n\right) & \phi\left(\xi - n\right) \\ 0 & 0 & \phi_{,\xi}\left(\xi - n\right) \end{bmatrix} \cdot \begin{Bmatrix} \hat{u}_n^0 \\ \hat{w}_n^0 \\ \hat{\beta}_{xn} \end{Bmatrix} \quad (25)$$

Incorporation of the approximated variables into Eq. (23) yields the following element stiffness and mass matrices

$$\left[\boldsymbol{K}_e^{kl}\right] = \begin{bmatrix} \frac{A_{11}}{l_e}\Gamma_{kl}^{11} & 0 & 0 \\ 0 & \frac{A_{55}}{l_e}\Gamma_{kl}^{11} & A_{55}\Gamma_{kl}^{01} \\ 0 & A_{55}\Gamma_{kl}^{10} & A_{55}l_e\Gamma_{kl}^{00} + \frac{D_{11}}{l_e}\Gamma_{kl}^{11} \end{bmatrix} \quad (26)$$

$$\left[\boldsymbol{M}_e^{kl}\right] = \boldsymbol{\rho} \cdot l_e \cdot \Gamma_{kl}^{00} \quad (27)$$

and the external surface load vector:

$$\boldsymbol{F}^k(t) = l_e \cdot \int_0^1 \bar{\tau}\left(\xi, t\right) \cdot \phi\left(\xi - k\right) d\xi \quad (28)$$

Again, the total matrices may be assembled from the element ones using Eq. (23) yielding the discrete system of equation as in Eq. (10).

3.4 Developement of a FWD High-Order Beam Element

The FWD method is finally employed within the analysis of dynamic response in thick beams and the highly demanding task of simulating ultrasonic antisymmetric and symmetric straight-crested guided waves. For this purpose, the FWD method is combined with a High-Order Laminate Theory (HOT) developed by the authors

[Plagianakos and Saravanos (2009)]. In order to make this paper self-consistent, the basic points of this theory are briefly presented. HOT assumes cubic variation of the axial and transverse displacements *u* and *w*, as follows,

$$u(x,z,t) = u^1(x,t)\,\Psi^1(\zeta) + u^2(x,t)\,\Psi^2(\zeta) - \gamma_x(x,t)\,\frac{\zeta^2 - 1}{2} - \delta_x(x,t)\,\zeta\,\frac{\zeta^2 - 1}{6}$$

(29)

$$w(x,z,t) = w^1(x,t)\,\Psi^1(\zeta) + w^2(x,t)\,\Psi^2(\zeta) - \gamma_\zeta(x,t)\,\frac{\zeta^2 - 1}{2} - \delta_\zeta(x,t)\,\zeta\,\frac{\zeta^2 - 1}{6}$$

(30)

where the coefficients u^1, w^1, u^2, w^2 denote the displacements at the bottom and top surfaces respectively; γ and δ are hyper-rotations of the strip [Saravanos and Heyliger (1995)]; $\zeta = \frac{2z}{h}$ is a normalized thickness coordinate; $\Psi^1(\zeta) = \frac{1-\zeta}{2}$ and $\Psi^2(\zeta) = \frac{1+\zeta}{2}$. HOT effectively represents 2D plane strain conditions in the cross section of the beam and provides approximations of the axial (ε_x), transverse (ε_z) and shear (ε_{xz}) strain, as derived from Eqs. (31)-(33).

$$\varepsilon_1 \equiv \varepsilon_x = \frac{u_{,x}^1 + u_{,x}^2}{2} + \frac{\gamma_{x,x}}{2} + \left(\frac{u_{,x}^1 - u_{,x}^2}{2} + \frac{\delta_{x,x}}{6} \right) \cdot \zeta - \frac{\gamma_{x,x}}{2} \cdot \zeta^2 - \frac{\delta_{x,x}}{6} \cdot \zeta^3$$

(31)

$$\varepsilon_3 \equiv \varepsilon_z = \frac{w^2 - w^1}{h} + \frac{\delta_z}{3h} - \frac{2\gamma_z}{h} - \frac{\delta_z}{h}\zeta^2$$

(32)

$$\varepsilon_5 \equiv \varepsilon_{xz} = \frac{u^2 - u^1}{h} + \frac{w_{,x}^1 + w_{,x}^2}{2} + \frac{\gamma_{z,x}}{2} + \frac{\delta_x}{3h} +$$
$$\left(\frac{w_{,x}^2 - w_{,x}^1}{2} - \frac{2\gamma_x}{h} + \frac{\delta_{z,x}}{6} \right) - \left(\frac{\gamma_{z,x}}{2} + \frac{\delta_x}{h} \right) \cdot \zeta_n^2 - \frac{\delta_{z,x}}{6} \cdot \zeta_n^3$$

(33)

3.4.1 Generalized Equations of Equilibrium and Laminate Matrices

According to the principle of virtual work the equations of motion are expressed as:

$$\int_0^l \left\{ \int_{-\frac{h}{2}}^{\frac{h}{2}} \delta\boldsymbol{\varepsilon}^T \cdot [\boldsymbol{Q}_C] \cdot \boldsymbol{\varepsilon}\, dz + \int_{-\frac{h}{2}}^{\frac{h}{2}} \delta u \cdot (-\rho\ddot{u}) + \delta w \cdot (-\rho\ddot{w})\, dz + [\delta\bar{u} \cdot \tau_{xz} + \delta\bar{w} \cdot \tau_z]_{-\frac{h}{2}}^{\frac{h}{2}} \right\} dx = 0$$

(34)

where $[\boldsymbol{Q}_C]$ is the stiffness matrix of a an orthotropic composite ply and ρ is the mass density. Incorporation of Eqs. (31)-(33)into (34) leads to

$$\int_0^l \left(\delta\boldsymbol{\varepsilon}_L^T \cdot [\boldsymbol{K}_L] \cdot \boldsymbol{\varepsilon}_L \right) dx + \int_0^l \left(\delta\boldsymbol{U}_L^T \cdot [\boldsymbol{\rho}_L] \cdot \boldsymbol{U}_L \right) dx + [\delta\bar{u} \cdot \tau_{xz} + \delta\bar{w} \cdot \tau_z]_{-\frac{h}{2}}^{\frac{h}{2}} = 0 \quad (35)$$

where $[K_L]$ is the generalized stiffness matrix of the laminate and $[\rho_L]$ is the generalized laminated density matrix:

$$[K_L] = \begin{bmatrix} [K_{L_{11}}] & [K_{L_{13}}] & 0 \\ [K_{L_{13}}]^T & [K_{L_{33}}] & 0 \\ 0 & 0 & [K_{L_{55}}] \end{bmatrix} \tag{36}$$

The subscripts "11", "33", "55" and "13" denote the axial, transverse, shear and coupling stiffness terms, respectively. The laminate stiffness submatrices are further related to generalized laminate stiffness coefficients,

$$[K_{L_{11}}] = \begin{bmatrix} A_{11} & B_{11} & D_{11} & E_{11} \\ & D_{11} & E_{11} & F_{11} \\ & & F_{11} & G_{11} \\ sym & & & H_{11} \end{bmatrix} \tag{37}$$

$$[K_{L_{13}}] = \begin{bmatrix} A_{13} & B_{13} & D_{13} \\ B_{13} & D_{13} & E_{13} \\ D_{13} & E_{13} & F_{13} \\ E_{13} & F_{13} & G_{13} \end{bmatrix} \tag{38}$$

$$[K_{L_{33}}] = \begin{bmatrix} A_{33} & B_{33} & D_{33} \\ & D_{33} & E_{33} \\ sym & & F_{33} \end{bmatrix} \tag{39}$$

$$[K_{L_{55}}] = \begin{bmatrix} A_{55} & B_{55} & D_{55} & E_{55} \\ & D_{55} & E_{55} & F_{55} \\ & & F_{55} & G_{55} \\ sym & & & H_{55} \end{bmatrix} \tag{40}$$

where

$$\langle A_{ij}, B_{ij}, D_{ij}, E_{ij}, F_{ij}, G_{ij}, H_{ij} \rangle = \frac{h}{2} \sum_{k=1}^{N_p} \int_{\zeta_k}^{\zeta_{k+1}} [Q_{Cij}] \langle 1, \zeta, \zeta^2, \zeta^3, \zeta^4, \zeta^5, \zeta^6 \rangle d\zeta \tag{41}$$

where N_p is the number of plies and ζ_k, ζ_{k+1} are the normalized thickness coordinates at the bottom and top face of each ply.

After expressing the generalized laminate DOFs in extended vector notation, i.e. $U_L = [u^1, u^2, w^1, w^2, \gamma_x, \gamma_z, \delta_x, \delta_z]^T$, their wavelet interpolation along the x-axis takes the form,

$$U_L(x,t) = \sum_{n=-(L-2)}^{0} \hat{U}_{Ln}(t) \cdot \phi(\xi - n) \tag{42}$$

Combining Eqs. (36)-(41) into Eq. (42) the elemental stiffness and mass matrices are derived. Their explicit expressions are shown in the Appendix.

3.5 Boundary Constraints for Displacements

The equation of motion Eq. (10) is solved in the domain of wavelet coefficients, however, all boundary conditions are imposed on the physical degrees of freedom. The link between the physical DOFs and the unknown wavelet coefficients is provided by Eq. (5), therefore, each constraint on a physical DOF imposes an equality constraint, also known as multi-point constraint in FEA literature, between the unknown wavelet coefficients in the domain of support. There are many direct and indirect methods proposed in the literature for the application of equality constraints, however, we take advantage of the finite support range in Eq. (5) to propose a method which is applicable to any physical DOF. In brief and without loss of generality, the application of the physical constraint $u_k(t) = u(x_k, t)$ at the grid point k is illustrated.

Application of Eq. (5) yields

$$u(x_k, t) = \hat{u}_{k-1}(t) \cdot \phi(-1) + \sum_{n=-(L-2)}^{-2} \hat{u}_{k-n}(t) \cdot \phi(-n) \tag{43}$$

Solving Eq. (43) for $\hat{u}_{k-1}$:

$$\hat{u}_{k-1}(t) = \frac{1}{\phi(-1)} \cdot \left(u_k(t) - \sum_{n=-(L-2)}^{-2} \hat{u}_{k-n}(t) \cdot \phi(-n) \right) \tag{44}$$

Based on Eq. (44), the $L-2$ wavelet coefficients in the support domain of the constraint node k, are related to the physical DOF by a square matrix $\boldsymbol{R}_{BC}^k$:

$$[\hat{u}_{k-1}, \hat{u}_{k-2}, \ldots, \hat{u}_{k-L+2}]^T = \left[\boldsymbol{R}_{BC}^k \right] \cdot [\hat{u}, \hat{u}_{k-2}, \ldots, \hat{u}_{k-L+2}]^T \tag{45}$$

The later is exploited to replace the wavelet coefficient at the node preceding the application node of the physical constraint, by the physical DOF. The replacement involves only the range of $L-2$ wavelet coefficients in the support domain of node k. Considering the diagonal and banded structure of the mass and stiffness matrices respectively, only a small subset of $L-2$ equations of motion corresponding to the support of node k is involved. In general the application of Eq. (45) yields new stiffness, mass and force submatrices of the following form

$$\left[\boldsymbol{R}_{BC}^k \right]^T \cdot \left[\boldsymbol{M}^{kk} \right] \cdot \left[\boldsymbol{R}_{BC}^k \right] \cdot \ddot{\tilde{\boldsymbol{U}}}_k(t) + \left[\boldsymbol{R}_{BC}^k \right]^T \cdot \left[\boldsymbol{K}^{kk} \right] \cdot \left[\boldsymbol{R}_{BC}^k \right] \cdot \tilde{\boldsymbol{U}}_k(t) = \left[\boldsymbol{R}_{BC}^k \right]^T \cdot \boldsymbol{F}^k(t) \tag{46}$$

where $\tilde{\boldsymbol{U}}_k = [u_k, \hat{u}_{k-2}, \ldots, \hat{u}_{k-L+2}]^T$ and superscript k indicates the subset of $L-2$ equations of motion corresponding to the wavelet coefficients in the support domain of node k. After the replacement, the physical constraint is eliminated from

the subsystem of Eq. (46). The previous method for the application of boundary conditions, is easily repeated and applied to other physical DOFs, causes minimal disturbance in the structure of the mass and stiffness matrices and is computationally efficient.

3.6 Time Integration

As previously discussed, one of the main advantages of the FWD method is its capability to provide near diagonal consistent mass matrices. This feature yields a clear advantage in the development of fast and accurate explicit time integration schemes, as traditional FEM employs lump-mass matrices to achieve mass diagonalization, which in turn leads to loss of accuracy. The discrete system of the equations of motion Eq. (10) is solved employing the central difference explicit integration scheme, i.e.

$$\frac{1}{\Delta t^2} \cdot [\boldsymbol{M}] \cdot \boldsymbol{U}(t + \Delta t) = \boldsymbol{R}(t) \tag{47}$$

$$\boldsymbol{R}(t) = \boldsymbol{F}(t) - \left([\boldsymbol{K}] - \frac{2}{\Delta t^2}[\boldsymbol{M}]\right) \cdot \boldsymbol{U}(t) - \frac{1}{\Delta t^2} \cdot [\boldsymbol{M}] \cdot \boldsymbol{U}(t - \Delta t) \tag{48}$$

Solution of the later requires inversion of the mass matrix in every time step for the calculation of $\boldsymbol{U}(t + \Delta t)$. Considering the structure of the FWD mass matrix shown in Figure 7, the solution of the above system is divided in two independent stages. The $N - 2 \cdot (L - 1)$ rows of Eq. (47) are uncoupled and can be rapidly and separately calculated without inversion. The mass coupled $2 \cdot (L - 1) \times 2 \cdot (L - 1)$ part of the above system requires inversion to be solved, but its size is very small and has very little impact on the computational speed. Hence, the solution of Eq. (47) is expected to be much faster and accurate compared to traditional FEM.

4 Numerical Results

The efficiency of the introduced FWD method is evaluated using cases focused on the prediction of guided wave propagation in isotropic (Aluminum) rods and strips. These evaluations quantify the accuracy and computational efficiency of the proposed approach. The simulation of ultrasonic guided waves is a very challenging task, since it typically requires fine spatial discretization to capture the high wavenumbers, and the pursued dispersive characteristics and group velocity suffer from many numerical issues. The results of the FWD method are compared to traditional explicit FEA using 2-node and 3-node FEs. Geometry parameters and material properties are provided in Table 1.

All strip cases are considered clamped at their left- and free at their right-end respectively. Waves are excited by application of a concentrated force on the free end

Table 1: Material Properties and Geometric Parameters of Aluminum Specimen.

Quantity	Symbol	Value	Units
Axial Modulus	E_1	70.0	GPa
Transverse Modulus	E_3	70.0	GPa
Shear Modulus	G_{13}	26.9	GPa
Poisson's ratio	v_{13}	0.34	
Density	ρ	2,700	$kg \cdot m^{-3}$
Length	L	6	m
Width	W	1	m
Thickness	t	0.06	m

in the form of a Hanning windowed pulse of central frequency 15 kHz (Figure 8). The maximum amplitude is arbitrarily - and without loss of generality - selected to be $0.5N$ for rods and shear beams, and $1N$ for HOT beam models respectively.
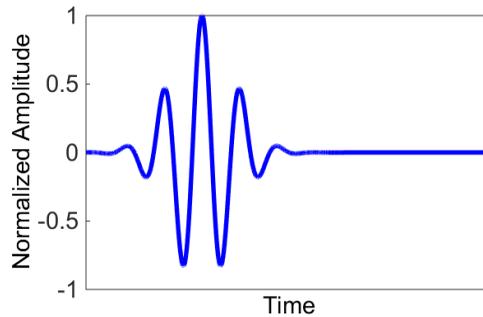
Figure 8: Applied Excitation; Normalized Amplitude is Employed.

Wave propagation is simulated using DB3, DB6 and DB12 FWD elements; DB18 is also employed, but only as a demonstrator for the HOT beam model. Convergence is determined by comparing the obtained solutions to a reference response, obtained by a rigorous model employing DB12 FWD elements with 1200 nodes. Each investigated model is considered to have converged, when the RMS error with respect to the reference solution is lower than 2%. This criterion ensures that the achieved accuracy in convergence is comparable for all models. There is a minimum number of nodes (grid points) associated with the central wavenumber or wavelength of a certain wave packet, not with the central frequency, which relates to the order of DB wavelet. The relationship to the central frequency - wavenumber is implicit and provided by the dispersion equation of the respective structural dynamics problem. On the other hand, the computational efficiency of each FWD

Table 2: Simulation of a longitudinal wave in a rod structure; Minimum number of nodes and respective solution time needed for each model to converge.

Element Type	Number of Nodes	Solution Time (s)
DB12	99	0.36
DB6	130	0.55
DB3	404	2.61
3-node FE	250	1.85
2-node FE	1000	16.3

element is reflected on the number of nodes and the size of each model being investigated. The computation time required by each FWD model to achieve converge with a 2% RMS error is also monitored.

4.1 Wave Propagation in Rods

An aluminum rod with length $l = 6$ m is investigated. This is the simpler case of ultrasonic wave simulation, because the longitudinal waves are non-dispersive and the rod finite element does not suffer from shear locking; hence the main challenge is the modeling of the small wavelengths. As shown in Figure 9, all FWD and FE models finally converge to identical predictions, however, the DB6 and DB12 FWD models require substantially coarser discretization and lower computational time to converge compared (Table 2).
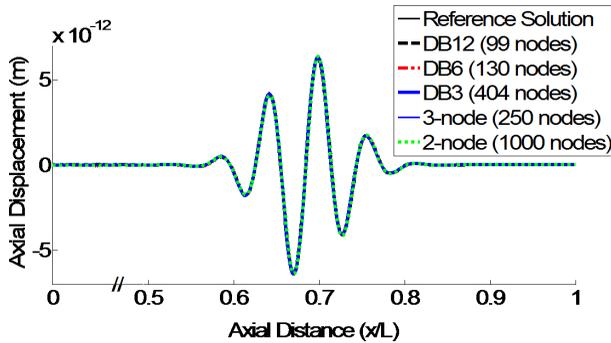
Figure 9: Predicted transient wave response of a rod structure at t=0.705 ms upon convergence of all FWD elements. Numbers in parenthesis indicate number of nodes required for convergence with a 2% RMS error.

The superiority of the DB12 FWD model is demonstrated in Figure 10, which

presents the predictions using a coarse discretization of 99 nodes. The DB12 element has already converged, while the 2-node and 3-node finite elements yield artificial dispersion and erroneous group velocity/amplitude.
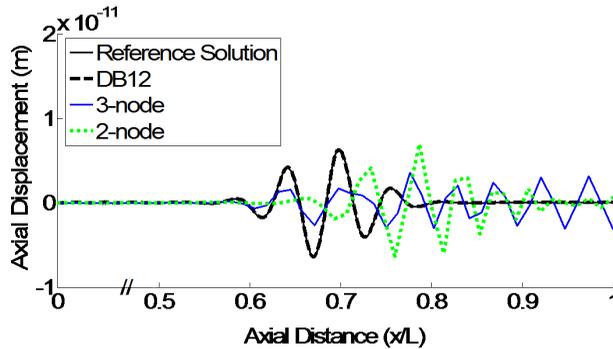
Figure 10: Predicted transient wave response in an Aluminum rod using a uniform grid of 99 nodes. The superiority of DB12 FWD Elements vs traditional FE models is demonstrated.

In order to better support this observation, a convergence study for the FWD elements is shown in Figure 11, which presents the respective RMS error with respect to the reference solution vs. the number of the nodes implemented in each FWD and FE model. Figure 11 reveals that as the order of the wavelet increases, the convergence of the FWD models is improved dramatically. The 3-node FE seems to be slightly better than the DB3-based FWD Element. The advantage of using FWD element appears when the wavelet order increases. Clearly, the DB6 and D-B12 based elements converge much faster than the traditional FEs. As intuitively expected, the benefits of the FWD method are realized from its capability to utilize higher order WSF without altering the discretization.
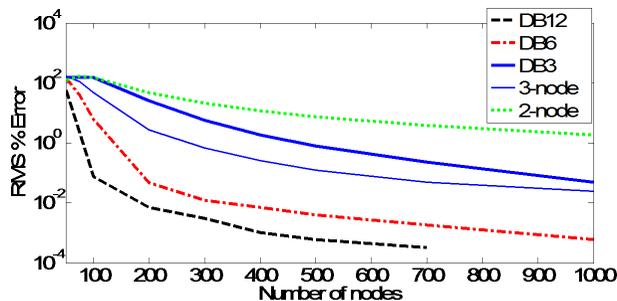
Figure 11: Resultant RMS error vs. number of nodes for the Rod Structure modeled with FWD and FEA elements.

Table 3: Simulation of a wave in a Timoshenko Beam; Minimum number of nodes and respective solution time needed for each model to converge.

Element Type	Number of Nodes	Solution Time (s)
DB12	197	10.10
DB6	290	34.84
3-node FE	450	69.47
2-node FE	1250	712.68

4.2   *Wave Propagation is Timoshenko Shear Beams*

The same structure is considered as a shear beam model with rotational inertia. The structure is subjected to transverse loading and simulated using the developed FWD shear elements. The beam is transversely excited at its free end by a pair of antisymmetric concentrated forces which excites the first antisymmetric wave mode (A_0). The simulation of an antisymmetric guided wave is more challenging compared to the longitudinal axial wave; not only because smaller wavelengths appear, but also because the dispersive nature of A_0 has to be handled. First-order shear finite elements typically exhibit shear locking, therefore, selectively reduced integration is used in the calculation of the shear stiffness submatrices of the finite elements.

Figure 12 shows predicted snapshots of the transverse displacement w^0 at an arbitrary time ($t = 0.696$ ms) predicted by DB6 and DB12 FWD models, and 2-node and 3-node finite element models. Again, convergence is assumed when the RMS error get lower than 2%. The required number of uniformly spaced nodes and the computation time needed for each model to converge is shown in Table 3. The DB6 and DB12 FWD elements exhibit superior spatial convergence. The attained convergence rates for each FWD beam element are shown in Figure 13. The FWD method shows improved convergence with respect to the 2-node and 3-node finite elements in the simulation of the A_0 wave as compared to the previous case of longitudinal waves.

The superiority of the DB12 FWD element against the 3- and 2-node traditional FEs is restated in Figure 14, which shows predicted snapshots using a uniform a grid of 197 nodes. While the DB12 element provides excellent prediction of the A_0 wavepacket, the FE models provide inferior predictions with lower amplitude and artificial dispersion.

The previous numerical results strongly support the high accuracy and computational efficiency of high order wavelet elements (DB6 and DB12) vs. traditional FEs. Interestingly, the FWD method appears to be free of spurious shear overstiff-
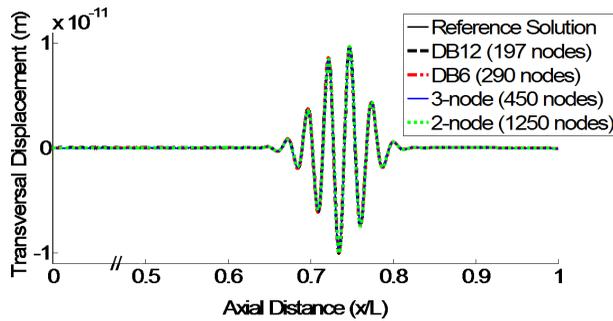
Figure 12: Predicted transient wave response of a Timoshenko Beam structure at $t = 0.696$ ms upon convergence of all FWD elements. Numbers in parenthesis indicate number of nodes required for convergence with a 2% RMS error.
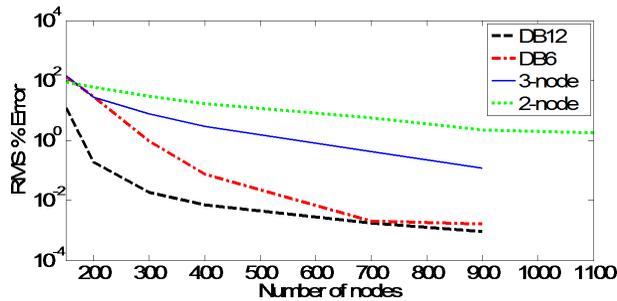
Figure 13: Resultant RMS error vs. number of nodes for beam structure modeled with FWD and FEA shear beam elements.
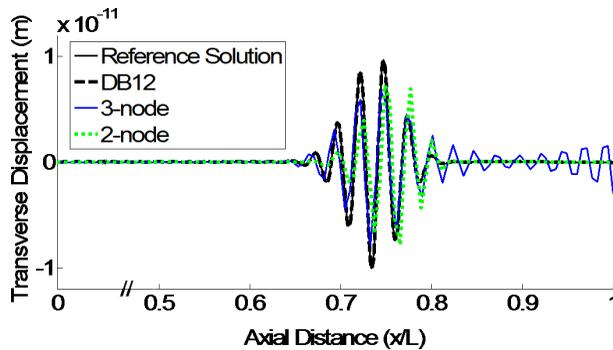
Figure 14: Predicted transient wave response in a Timoshenko beam by a DB12 FWD vs traditional FEs models using a uniform grid of 197 nodes.

ening, thus, offering another advantage compared to the shear beam finite elements.

Table 4: Simulation of a wave in a High Order Beam; Minimum number of nodes and respective solution time needed for each model to converge.

Element Type	Number of Nodes	Solution Time (s)
DB18	191	231
DB12	202	264
DB6	310	703
3-node FE	630	2,304
2-node FE	1500+	21,600+

4.3 Wave Propagation in High-Order Beams

The previous model has been upgraded to include high-order theory (HOT) beam FWD elements. Performance evaluations include the simulation of the first symmetric (S_0) and anti-symmetric (A_0) waves. The FWD results are compared with predictions of 2-node and 3-node HOT finite elements with reduced stiffness integration.

Figure 15 presents snapshots of the transient beam response at $t = 0.7002$ ms, as predicted by various models. All models have converged according to the 2% RMS criterion and contain both the S_0 and A_0 wave packets. As in the previous cases, the DB12 and DB6 FWD models have converged in the simulation of waves using substantially lower number of nodes compared to the finite elements (Table 4).
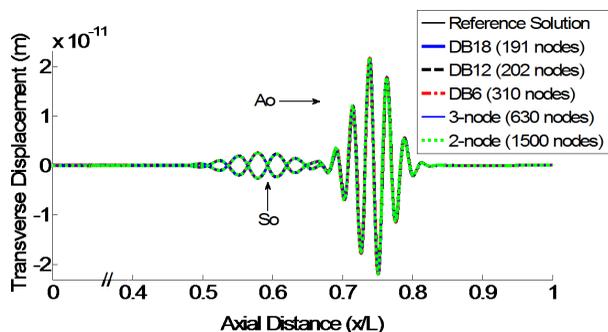
Figure 15: Predicted transient wave response of a HOT Beam structure at t=0.7002 ms upon convergence of all FWD elements. Numbers in parenthesis indicate number of nodes required for convergence with a 2% RMS error.

As seen in in Figure 16, the high-order beam theory is rather computationally demanding, however the difference in the convergence rates of the HOT FWD beam

models vs. the FE models is higher than in the case of Timoshenko beams.
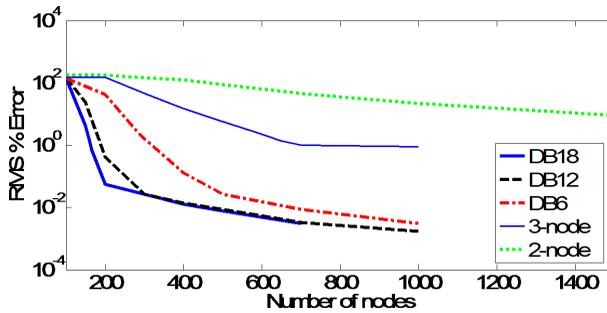
Figure 16: Resultant RMS error vs. number of nodes for the beam structure modeled with FWD and FEA HOT beam elements.

Figure 17 presents the excellent simulation of the S_0 and A_0 wavepackets obtained by the DB12 FWD of only 202 nodes. On the other hand, the traditional FEs produce only errors and artificial dispersion for the same number of nodes. Moreover, the 2-node element does not achieve convergence even if more than 1500 nodes are used.
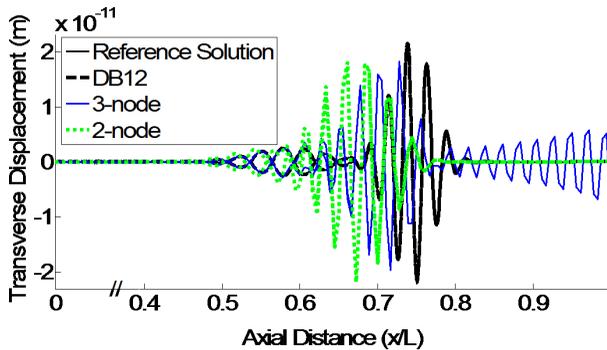
Figure 17: Predicted transient wave response in a HOT beam by a DB12 FWD vs traditional FEs models using a uniform grid of 202 nodes.

Figures 16 also illustrates the convergence of the FWD HOT element with higher order (DB18) scaling function. Figure 18 shows a comparison between DB12 and DB18 Daubechies wavelet at the minimum number of nodes that DB18 requires to converge.

Both figures show that the implementation of the DB18 scaling function yields additional gains in the number nodes required for convergence compared to DB12.
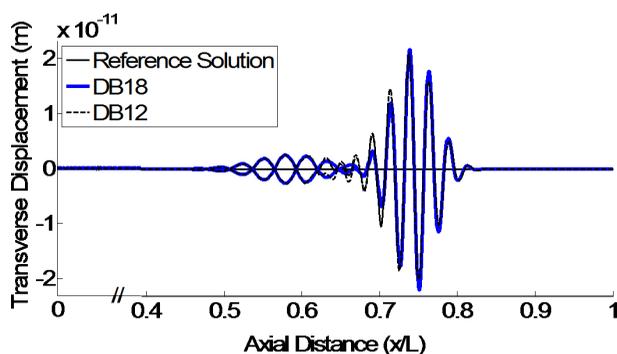
Figure 18: Predicted transient wave response in a HOT beam by a DB18 FWD vs DB12 model using a uniform grid of 191 nodes.

The obtained results in Figure 16 also suggest that the effectiveness of the presented method above a certain order of Daubechies scaling function, in this case DB12, may be reduced. The procedure for increasing the order of Daubechies scaling functions remained the same, but as the order of Daubechies scaling functions increases the ill-condition of the matrices is also increasing. We found evidence that the process of wavelet order promotion can be enhanced by improving the method of calculation of the connection coefficients; however this is beyond the scope of the current work and may be addressed in the future.

In addition to the high spatial convergence rate illustrated in Figure 16, the FWD method requires substantially less computation time than traditional FEs for the simulation of all previous wave propagation cases, as shown in Table 4. This is primarily attributed to two factors: (1) the nearly-diagonal mass matrices obtained by the FWD models, which boosts the speed of explicit integration; and (2) the substantially lower numbers of nodes and DOFs required for convergence, which reduces the size of the discrete problem. Table 5 provides the computation time required for the simulation of the previous cases, using the same number of nodes in all models.

The results in Table 5 indicate that a substantial computational speedup is obtained during the explicit time integration phase due to the near diagonal mass matrices of the FWD models vs. the FEs, which increases with the size of the discretization. In closing, the overall computational time required to obtain converged solutions in each case of wave propagation predictions are overviewed in Figure 19. Apparently, the gains in computation time obtained by the DB12, also by the DB6 FWD, elements are dramatic compared to the finite elements. As the problem complexity increases, these benefits become clearer. For example, the simulation of A_0 and S_0

Table 5: Time needed for time integration through number of nodes between DB12 and 3-node HOT beam elements.

Number of Nodes	DB12	3-node FE	Difference
222	55.2	63.3	8.1
322	100.8	142.5	41.7
422	156.3	248.9	92.6
522	221.7	381.4	159.7
622	292.9	562.8	269.9
722	373.1	749.4	376.3
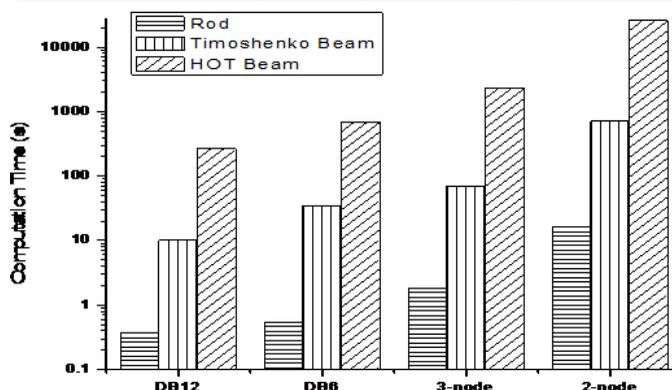
Figure 19: Computation time needed (logarithmic scale) for converged solutions of rod and beam structures modeled by each type of element.

waves using the DB12 FWD HOT beam element (Case 3) is nearly 10 times faster than the respective 3-node finite element and 100 times faster than the respective 2-node element.

5 Conclusions

Taking advantage of the appealing properties of Daubechies wavelets, a novel wavelet-based method, termed as finite wavelet domain (FWD) method has been developed for the prediction of high-frequency transient dynamic responses and guided wave propagation in rods and strips. Formulations of the FWD method in the context of rod, first shear order and high-order beam theory were employed, and wavelet-based elements were developed. Demonstration cases establish the ultra-high convergence rate and the tremendous speed-up that emanates from Daubechies wavelets, even in demanding cases, such as the simulation of symmetric and anti-symmetric waves using a high-order beam theory. Two key advantages are demonstrated: (1) the ability to increase the order of approximation and computational

speed (p-method) without remeshing; and (2) the amenability of the FWD method to explicit formulations because of the consistent nearly-diagonal mass matrices. The higher order FWD elements are shown to perform much better than the lower order elements (DB12 vs. DB6); however, both outperform drastically traditional 2-node and 3-node finite elements. The developed FWD method has shown tremendous potential for application in demanding transient dynamic simulations, such as the analysis of Lamb wave-based SHM and NDE systems. Future work focus on the expansion of the method to laminated composite plate structures and 2D spatial interpolation problems.

References

Bathe, K. J. (1996):   *Finite Element Procedures*. Prentice Hall, New Jersey.

Beylkin, G. (1992):   On the representation of operators in bases of compactly supported wavelets. *SIAM Journal on Numerical Analysis*, vol. 29, no. 6, pp. 1716–1740.

Burgos, R. B.; Santos, M. A. C.; e Silva, R. R. (2013):   Deslauriers–dubuc interpolating wavelet beam finite element. *Finite Elements in Analysis and Design*, vol. 75, pp. 71–77.

Burgos, R. B.; Santos, M. A. C.; e Silva, R. R. (2015):   Analysis of beams and thin plates using the wavelet-galerkin method. *International Journal of Engineering and Technology*, vol. 7, no. 4, pp. 261.

Chen, M.-Q.; Hwang, C.; Shih, Y.-P. (1996):   The computation of wavelet-galerkin approximation on a bounded interval. *International Journal for Numerical Methods in Engineering*, vol. 39, no. 17, pp. 2921–2944.

Chen, X.; He, Z.; Xiang, J.; Li, B. (2006):   A dynamic multiscale lifting computation method using daubechies wavelet. *Journal of Computational and Applied Mathematics*, vol. 188, no. 2, pp. 228–245.

Daubechies, I. (1992):   *Ten Lectures on Wavelets*. Society for Industrial and Applied Mathematics, Philadelphia, PA, USA.

Delsanto, P. P.; Scalerandi, M. (1998): A spring model for the simulation of the propagation of ultrasonic pulses through imperfect contact interfaces. *The Journal of the Acoustical Society of America*, vol. 104, no. 5, pp. 2584–2591.

Dempster, M. A.; Eswaran, A. (2001): *Solution of PDEs by Wavelet Methods*. University of Cambridge.

Díaz, L. A.; Martín, M. T.; Vampa, V. (2009): Daubechies wavelet beam and plate finite elements. *Finite Elements in Analysis and Design*, vol. 45, no. 3, pp. 200–209.

Katsikadelis, J. T. (2002): *Boundary Elements: Theory and Applications*. Elsevier.

Kessler, B. M.; Payne, G. L.; Polyzou, W. N. (2008): Wavelet notes. University of Iowa, 2008.

Ko, J.; Kurdila, A.; Pilant, M. (1995): A class of finite element methods based on orthonormal, compactly supported wavelets. *Computational Mechanics*, vol. 16, no. 4, pp. 235–244.

Li, B.; Chen, X. (2014): Wavelet-based numerical analysis: a review and classification. *Finite Elements in Analysis and Design*, vol. 81, pp. 14–31.

Lin, W.; Kovvali, N.; Carin, L. (2005): Direct algorithm for computation of derivatives of the daubechies basis functions. *Applied mathematics and computation*, vol. 170, no. 2, pp. 1006–1013.

Ma, J.; Xue, J.; Yang, S.; He, Z. (2003): A study of the construction and application of a daubechies wavelet-based beam element. *Finite Elements in Analysis and Design*, vol. 39, no. 10, pp. 965–975.

Mitra, M.; Gopalakrishnan, S. (2005): Spectrally formulated wavelet finite element for wave propagation and impact force identification in connected 1-d waveguides. *International Journal of Solids and Structures*, vol. 42, no. 16, pp. 4695–4721.

Monasse, P.; Perrier, V. (1998): Orthonormal wavelet bases adapted for partial differential equations with boundary conditions. *SIAM Journal on Mathematical Analysis*, vol. 29, no. 4, pp. 1040–1065.

Patera, A. T. (1984): A spectral element method for fluid dynamics: Laminar flow in a channel expansion. *Journal of Computational Physics*, vol. 54, no. 3, pp. 468 – 488.

Patton, R.; Marks, P. (1995): Application of the rod wavelet finite element to dynamic systems. In *36th Structures, Structural Dynamics and Materials Confer-*

ence: Structures, Structural Dynamics, and Materials and Co-located Conferences. American Institute of Aeronautics and Astronautics.

Patton, R.; Marks, P. (1995): The rod finite element, a new type of finite element. In *36th Structures, Structural Dynamics and Materials Conference: Structures, Structural Dynamics, and Materials and Co-located Conferences*. American Institute of Aeronautics and Astronautics.

Plagianakos, T. S.; Saravanos, D. A. (2009): Higher-order layerwise laminate theory for the prediction of interlaminar shear stresses in thick composite and sandwich composite plates. *Composite Structures*, vol. 87, no. 1, pp. 23–35.

Qian, S.; Weiss, J. (1993): Wavelets and the numerical solution of boundary value problems. *Applied Mathematics Letters*, vol. 6, no. 1, pp. 47 – 52.

Rekatsinas, C.; Nastos, C.; Theodosiou, T.; Saravanos, D. (2014): A time-domain high-order spectral finite element for the simulation of symmetric and antisymmetric guided waves in laminated composite strips with active piezoresistive sensors. In *EWSHM-7th European Workshop on Structural Health Monitoring*, Nantes, France.

Rekatsinas, C.; Nastos, C.; Theodosiou, T.; Saravanos, D. (2015): A time-domain high-order spectral finite element for the simulation of symmetric and anti-symmetric guided waves in laminated composite strips. *Wave Motion*, vol. 53, pp. 1–19.

Saravanos, D. A.; Heyliger, P. R. (1995): Coupled layerwise analysis of composite beams with embedded piezoelectric sensors and actuators. *Journal of Intelligent Material Systems and Structures*, vol. 6, no. 3, pp. 350–363.

Strikwerda, J. C. (2004): *Finite difference schemes and partial differential equations*. Siam.

Theodosiou, T.; Nastos, C.; Rekatsinas, C.; Saravanos, D. (2014): Finite wavelet domain method for efficient modeling of lamb wave based structural health monitoring. In *EWSHM-7th European Workshop on Structural Health Monitoring*, Nantes, France.

Xiang, J.; Liang, M. (2011): Multiple damage detection method for beams based on multi-scale elements using hermite cubic spline wavelet. *Computer Modeling in Engineering & Sciences*, vol. 73, no. 3, pp. 267–298.

Xiang, J.; Matsumoto, T.; Wang, Y.; Jiang, Z. (2011): A hybrid of interval wavelets and wavelet finite element model for damage detection in structures. *Computer Modeling in Engineering & Sciences*, vol. 81, no. 3, pp. 269–294.

Xiang, J.; Wang, Y.; Jiang, Z.; Long, J.; Ma, G. (2012): Numerical simulation of plane crack using hermite cubic spline wavelet. *Computer Modeling in Engineering & Sciences*, vol. 88, no. 1, pp. 1–16.

Zhang, T.; Tian, Y.-C.; Tade, M. O.; Utomo, J. (2007): Comments on the computation of wavelet-galerkin approximation on a bounded interval. *International Journal for Numerical Methods in Engineering*, vol. 72, no. 2, pp. 244–251.

Appendix

Calculation of DB WSFs

As already mentioned there are no explicit expressions for DB WSF. Instead, they can be calculated at special points, namely the "dyadic points", using the dilation equation

$$\phi \left(2^j \cdot x \right) = \sqrt{2} \cdot \sum_{k=0}^{L-1} h_k \cdot \phi \left(2^{j+1} \cdot x - k \right) \tag{49}$$

Following Eq. (49) a DB WSF at resolution j is uniquely defined by a set of "filter coefficients" (h_k). The number (L) of filter coefficients determines the "order of the wavelet" and is required to be an even integer. Each WSF is named based on its order using the notation *DBn*, where $n = \frac{L}{2}$. Clearly, L defines the support of the WSF. An interesting remark from the previous equation is that any WSF can be constructed as a linear combination of translated and dilated instances of the same WSF at a finer resolution. For resolution $j = 0$, this leads to the following homogeneous system of equations:

$$\{\boldsymbol{\phi}_i\} = \left[\sqrt{2} h_{2i-k} \right] \cdot \{\boldsymbol{\phi}_k\}, \ i,k \in \mathbb{N} : i,k \leq L-1 \tag{50}$$

which provides the values of the WSF. This is an eigenvalue problem, satisfied by the eigenvector corresponding to the eigenvalue $\lambda = 1$. The generic solution has to be scaled using the normalization condition:

$$\int_{-\infty}^{\infty} \phi \left(x \right) dx = 1 \tag{51}$$

After the WSF has been calculated at resolution $j = 0$, any other resolution can be calculated from Eq. (49) increasing progressively the value of j.

Calculation of WSF Quadratures

As described in the next section, WSF quadratures in a bounded interval will be required. These are termed as "Connection Coefficients" and their generalized form

can be represented as:

$$\Gamma_{kl}^{m,n} \equiv [\Gamma_{kl}]^{m,n} = \int_0^1 \phi^{(m)}(\xi - k) \cdot \phi^{(n)}(\xi - l)\, d\xi \qquad (52)$$

where $\phi^{(i)}$ denotes the ith derivate of the scaling function. The lack of explicit expressions prohibits direct analytical integration. On the other hand, the highly-oscillatory nature of WSFs makes numerical integration computationally very expensive, because ultra-fine discretization is required. Fortunately, interesting works exist in literature that can be exploited towards the elevation of such numerical issues. Beylkin [Beylkin (1992)] has described exact and explicit representations for differential operators and shift operators in orthonormal bases. Chen, Hwang and Shih [Chen, Hwang, and Shih (1996)] have described exact evaluations of various connection coefficients, updated and corrected by Zhang, Tian, Tade and Utomo [Zhang, Tian, Tade, and Utomo (2007)].

Regarding the calculation of stiffness and mass matrices employing connection coefficients, Chen, He, Xiang and Li [Chen, He, Xiang, and Li (2006)] have presented an efficient method incorporating Eq. (49) into Eq. (52) and applying appropriate normalizing conditions. Following their approach, Eq. (52) can be cast into

$$\Gamma_{kl}^{m,n} = 2^{m+n-1} \sum_{s,t} \left(h_{s-2t} h_{t-2l} + h_{s-2s+1} h_{t-2l+1} \right) \Gamma_{st}^{m,n},\ k,l \in \mathbb{Z}^- : -2 \cdot (L-1) \le k,l \qquad (53)$$

Rearranging terms further leads to the following eigenvalue problem:

$$\left(2^{m+n-1}[\boldsymbol{A}] - [\boldsymbol{I}] \right) \cdot [\boldsymbol{\Gamma}]^{m,n} = 0 \qquad (54)$$

where $\boldsymbol{A}$ is the matrix of filter coefficients derived from Eq. (53) and $\boldsymbol{I}$ is the identity matrix. Again normalization conditions are required:

$$\frac{q!}{(q-m)!} \cdot \frac{w!}{(w-n)!} \cdot \frac{1}{q+w-m-n+1} = \sum_{k,l} c_k^q \cdot c_l^w \cdot \Gamma_{kl}^{m,n},\ q,w \in \mathbb{N} : q,w \le \frac{L}{2} - 1 \qquad (55)$$

In the previous equation, denotes the vanishing moments of the WSF defined as:

$$c_j^i = \langle x^i, \phi(x-j) \rangle \qquad (56)$$

In the same sense, projecting load vectors ($\boldsymbol{R}$) into wavelet space requires the calculation of integrals of the form:

$$R_k^m = \int_0^1 \xi^m \cdot \phi(\xi - k)\, d\xi,\ m \in \mathbb{N} : m \le \frac{L}{2} - 1 \qquad (57)$$

assuming polynomial representation of the applied load in the physical space. Eq. (57) is iteratively solved starting from $m = 0$, replacing the WSF with Eq. (49) and normalizing with

$$\frac{1}{q+1} = \sum_k c_k^q \cdot R_k^0. \tag{58}$$

After the basic solution is derived, the rest of the terms can be obtained by

$$\left(2^{m+1} I - \sum_{i,k} (h_{i-2k} + h_{i-2k+1}) \right) \cdot R_k^m = \sum_i h_{h_{i-2k+1}} \sum_{s=1}^m \binom{m}{s} R_i^{m-s} \tag{59}$$

which finally provides the load vector in wavelet space.

It is clear that the followed approach always leads to a respective eigenvalue problem. It has to be noticed that as the order of the WSF increases, the ill-conditioning of the eigenvalue problem and the resultant connectivity matrices seems to increase, thus affecting the quality of the solution. In such cases, special solvers may be required, a topic which exceeds the scope of this work and may be addressed in future work.

Stiffness and Mass Matrices for the HOT-based FWD Element

$$\left[K_e^{kl} \right] = \begin{bmatrix} K_{e11}^{kl} & K_{e12}^{kl} \\ K_{e21}^{kl} & K_{e22}^{kl} \end{bmatrix} \tag{60}$$

$$\left[M_e^{kl} \right] = \begin{bmatrix} \rho A l_e \frac{\Gamma_{kl}^{00}}{3} & M_e^{21} & 0 & 0 & -M_e^{21} & 0 & M_e^{71} & 0 \\ \rho A l_e \frac{\Gamma_{kl}^{00}}{6} & M_e^{11} & 0 & 0 & -M_e^{21} & 0 & -M_e^{71} & 0 \\ 0 & 0 & M_e^{11} & 0 & 0 & -M_e^{21} & 0 & M_e^{71} \\ 0 & 0 & M_e^{21} & M_e^{11} & 0 & -M_e^{21} & 0 & -M_e^{71} \\ -M_e^{21} & -M_e^{21} & 0 & 0 & 2\rho A l_e \frac{\Gamma_{kl}^{00}}{15} & 0 & 0 & 0 \\ 0 & 0 & -M_e^{21} & -M_e^{21} & 0 & M_e^{55} & 0 & 0 \\ -\rho A l_e \frac{\Gamma_{kl}^{00}}{90} & -\rho A l_e \frac{\Gamma_{kl}^{00}}{90} & 0 & 0 & 0 & 0 & 2\rho A l_e \frac{\Gamma_{kl}^{00}}{945} & 0 \\ 0 & 0 & -M_e^{71} & -M_e^{71} & 0 & 0 & 0 & M_e^{77} \end{bmatrix} \tag{61}$$

where h is the thickness and l_e is the element length.